PAPER

Experimental investigation of the dehumidification and decarburization performance of metal–organic frameworks in solid adsorption air conditioning

Liu Chen [ID] * and Famei Yang

Solid adsorption air conditioning systems use solid adsorption materials to co-adsorb water vapor and carbon dioxide, allowing the humidity and carbon dioxide concentration in the air-conditioned room to be controlled. Exploring the co-adsorption mechanism of H_2O and CO_2 is essential for the screening of adsorbent materials, system design, and system optimization in solid adsorption air conditioning systems. A fixed-bed adsorption–desorption device was built, and the dynamic adsorption properties of three MIL adsorbent materials MIL-101(Cr), MIL-101(Fe), and MIL-100(Fe) for co-adsorption of H_2O and CO_2 were studied. The results showed that all three MIL adsorbent materials are capable of performing co-adsorption of H_2O and CO_2 and meet the requirements of solid adsorption air conditioning systems. MIL-101(Cr) is recommended for solid adsorption air conditioners where dehumidification is the main focus, while MIL-100(Fe) is recommended for solid adsorption air conditioners where carbon removal is the main focus.

1. Introduction

Under the serious threat of global fossil energy depletion and environmental pollution, countries around the world are exploring the path of sustainable development. With the development of the economy and society, demands for air conditioning continue to increase. According to the statistical data, building energy consumption is 40–60% of China's total energy consumption, with air conditioning operations accounting for 50% of building energy consumption.[1,2]

Adults exhale about 18 L of CO_2 per hour in a quiet state. When the concentration of CO_2 in an air-conditioned room exceeds 0.1%, they will experience a headache and the electrolyte balance in the body is disrupted, causing blood acidosis, and at a CO_2 concentration of 2.0% to 3.0%, severe headache, respiratory distress and unresponsiveness will occur.[3–5] So, the air conditioning should be able to perform the following functions in summer: cooling, dehumidification and control of indoor CO_2 concentration. The traditional air conditioning system based on the principle of vapor-compression refrigeration cools the air below its dew point temperature in order to meet the needs of cooling and dehumidification at the same time, resulting in massive energy consumption.[6] In addition, the large supply of hot and humid outdoor fresh air for diluting

indoor CO_2 further contributes to the energy consumption of the air conditioning systems by up to 30% or more.[7]

The use of low-grade energy air conditioning is an effective way to alleviate dependence on fossil energy. Solid adsorption air conditioning systems (SAACs) is a kind of device which can use waste heat, solar energy and other low-grade energy to achieve the purpose of dehumidification and cooling. Compared with the traditional vapor compression systems, SAACs are of great interest because they do not consume large amounts of electricity and do not require the use of chlorofluorocarbons (CFCs), which pollute the atmosphere, as refrigerants.

Due to the high energy consumption of the traditional air conditioning system, SAACs are attracting more attention.[8,9] SAACs are energy efficient and environmentally friendly because they can be driven by solar energy, geothermal energy or waste heat and use water as a refrigerant.[10,11] SAACs composed of a solid adsorption unit for dehumidification and an evaporative cooling unit for cooling.[12]

The solid adsorption unit is a key component in the application of SAACs since it directly affects the dehumidification efficiency and system energy consumption.[13] One of the keys to the high energy efficiency of the solid adsorption unit is the adsorbing material.[14] Currently, the commonly used adsorbent materials are silica gel, zeolite and activated alumina. The major drawbacks of these adsorbent materials are a low adsorption capacity and a high regeneration temperature.[13] Therefore, the selection of new adsorbent materials and their

Energy School, Xi'an University of Science and Technology, Yanta Road, Xi'an 710054, P. R. China. E-mail: chenliu@xust.edu.cn; Fax: +86 29 85583143; Tel: +86 29 85583143

adsorption properties are the research focus of SAACs. The conventional solid adsorption unit are available in fixed bed, desiccant wheel, and desiccant coated heat exchangers. In fixed bed solid adsorption unit, desiccant granules are tightly packed on a fixed bed. Fixed-bed solids adsorption units have the outstanding advantage of simple design and easier fabrication.[14] The desiccant wheel has to be loaded with desiccant material onto a fiber paper carrier to achieve continuous dehumidification and regeneration.[15] Desiccant coated heat exchangers is where the desiccant is attached to the surface of the compact heat exchanger in order to enhance the dehumidification of the heat exchanger.[16]

Metal–organic frameworks (MOFs) have attracted much attention due to their large specific surface area, controllable structure and composition.[14] MOFs have been widely used for adsorption H_2O and CO_2.[17,18] MOFs are expected to be used for co-adsorption of H_2O and CO_2 in SAACs to reduce energy consumption for fresh air.

The MIL (MIL: Material Institut Lavoisier) series are the MOFs studied by Ferey's research group.[19] MIL-100 and MIL-101 have attracted the attention of many researchers.[20,21] MIL-100 and MIL-101 have abundant porosity and large specific surface area, possessing both micropores and mesopores, with most significant advantage being their high water stability.[22,23] MIL-101 and MIL-100 are potentially promising materials to be used for the co-adsorption of H_2O and CO_2 in SAACs due to their high specific surface area and very excellent stability.[24–27]

In the application of SAACs, the focus is on the H_2O adsorption capacity, water stability and cycling performance of adsorbent material. MIL-101(Cr) showed excellent water absorption capacity of 1.5–1.7 g g^{-1}.[28] Küsgens et al.[29] tested H_2O adsorption properties of various MOF, and the results showed that MlL-100(Fe) and MIL-101(Cr) had not only high hydrothermal stability, but also had high H_2O capacity, up to 0.80–1.28 g g^{-1}. Ehrenmann et al.[30] found that MIL-101(Cr) could adsorb and desorb H_2O at 40 °C and 90 °C, and the adsorption capacity of H_2O was still as high as 0.939 g g^{-1} after multiple cycles.

MIL-101 and MIL-100 have an excellent adsorption capacity on low concentrations of CO_2. MIL-101 and MIL-100 exhibited high CO_2 adsorption capacities of 40 mmol g^{-1} and 18 mmol g^{-1}, respectively.[31] Xian et al.[32] have reported that H_2O enhances CO_2 adsorption capacity of MIL-100(Fe), with a 150% increase in CO_2 adsorption capacity when the relative humidity of the air was varied from 0% to 50%.

Appropriate MOFs for in SAACs have been studied. MIL-101(Cr), MIL-101(Fe) and MIL-100(Fe) have high dehumidification performance, low regeneration temperature and good long-term stability.[33,34] However, there is more or less CO_2 in the air-conditioned room. When there are more people, the CO_2 concentration will exceed the standard. Similar to the traditional air conditioning system, the existing SAACs also use the dilution to control CO_2 concentration, resulting in a large amount of energy consumption.

The three MIL adsorbent materials (MIL-101(Cr), MIL-101(Fe) and MIL-100(Fe)) not only capture H_2O but also adsorb CO_2 from the air. There is an urgent need to investigate

the co-adsorption properties of H_2O and CO_2 on the three MIL adsorbent materials, which provides important guidance for new fixed bed solid adsorption unit in SAACs. The adsorbent material determine the design and operation effectiveness of the simultaneous dehumidification and decarburization device, so it is necessary to explore co-adsorption of H_2O and CO_2 of the adsorbent material in air conditioning environment. Three MIL adsorbent materials, MIL-101(Cr), MIL-101(Fe) and MIL-100(Fe), were selected as co-adsorbent material for dehumidification and decarburization. A fixed-bed adsorption–desorption device was built to explore the influence of air conditioning environment (temperature, humidity and CO_2 concentration) on the co-adsorption effect, with the aim of providing a reference for the design of simultaneous dehumidification and decarburization of three MIL adsorbent materials in a solid adsorption air conditioning system.

2. Experimental materials and method

2.1. Materials synthesis

2.1.1 Synthesis of MIL-101(Cr). MIL-101(Cr) was synthesized using hydrothermal synthesis procedures reported by Ferey et al. and the purification was carried out.[28] First, 4.00 g chromium(III) nitrate $Cr(NO_3)_3 \cdot 9H_2O$ and 1.64 g 1,4-benzene dicarboxylic acid H_2BDC were dissolved into 48 mL deionized water and stirred for 10 min. Then, 0.3 mL fluorhydric acid was added and stirred for an additional 10 min. The mixture was transferred into an autoclave reactor, kept at 220 °C for 8 h. When the mixture is cooled to room temperature, N,N-dimethylformamide (15 mL) was added, and the mixture was stirred for 30 min with a magnetic stirrer. After adding 100 mL of ethanol, the mixture was then added to an autoclave reactor and kept at 100 °C for 20 h. A NH_2F aqueous solution (30 mmol L^{-1}) was added and soaked at 60 °C for 10 h. Finally, the reaction mixture was filtered and washed with deionized water and finally dried at 150 °C for 12 h to obtain green MIL-101(Cr). The above products were mixed with 15 mL N,N-dimethylformamide and 100 mL ethanol for 30 min, and then put into the reaction kettle, heated at 100 °C for 20 h. 30 mmol L^{-1} NH_4F aqueous solution was added and stored at 60 °C for 10 h. The product was filtered, cleaned, and dried at 150 °C for 12 h to obtain a green MIL-101Cr.

2.1.2 Synthesis of MIL-101(Fe). MIL-101(Fe) was synthesized by solvent thermal method via adding iron alkoxides precursor solution and the purification was carried out.[35] 0.5 mmol $FeCl_3 \cdot 6H_2O$ was added into 15 mL ethylene glycol, stirring at 40 °C for a certain time, marked as Solution A. 1.24 mmol terephthalic acid and 2.5 mmol $FeCl_3 \cdot 6H_2O$ were added into 20 mL N,N-dimethylformamide, marked as Solution B. Solution A was poured into Solution B with stirring. Then it was transferred to Teflon-sealed autoclave and heated at 110 °C for 20 h. Upon cooling down the reactants to room temperature, MIL-101(Fe) was obtained through centrifugation and cleaning five times with N,N-dimethylformamide and absolute methanol. Moreover, The washed adsorbent was transferred to

a drying oven for vacuum drying for 12 h, and the drying temperature was 80 °C, MIL-101 (Fe) was obtained.

2.1.3 Synthesis of MIL-100(Fe). MIL-100(Fe) was synthesized using hydrothermal synthesis procedures and the purification was carried out.[36] 0.9713 g of iron powder, 2.4063 g of 1,3,5-benzene tricarboxylic acid, 700 μL of hydrofluoric acid and 665 μL of nitric acid were mixed in 70 mL distilled water. The mixture was placed in 100 mL Teflon lined autoclave and heated at 423 K for 24 h. The pH remains acidic (<1) throughout the synthesis. The light-orange solid product was recovered by filtration and washed with deionized water A treatment in hot deionised water (80 °C) for 3 h was applied to decrease the amount of residual trimesic acid (typically, 1 g of MIL-100(Fe) in 350 mL of water), then filtered and vacuum dried at 373 K for 12 h. Finally, MIL-100(Fe) was obtained.

2.1.4 Silica gel. The conventional dehumidification material for SAACs is mainly used silica gel (SG). In order to make comparison, the co-adsorption properties of H_2O and CO_2 on SG was investigated at the same time. The conventional dehumidification material SG (Type A) purchased from Qingdao Meirong silica gel desiccant Co., Ltd.

2.2. Materials characterization

N_2 adsorption–desorption isotherms were obtained using ASAP2020 at 77 K. The surface area was calculated by Langmuir and Brunauer–Emmett–Teller (BET) methods, and pore size was calculated using Barrett–Joyner–Hatenda (BJH) model. Powder X-ray diffraction (PXRD) patterns of three materials were obtained using a Bruker D8Advance X-ray automatic diffractometer with Cu Kα radiation. The test conditions were a tube pressure of 30 kV, a tube current of 30 mA, a scan speed of 2° per min, and a scan range of 2° to 50°. Before analyzing the crystal morphology and particle size distribution of the dehumidification material by scanning electron microscopy and energy dispersive spectrometer (SEM-EDS), the prepared dehumidification material samples were ground and dried. Before the test, the sample was sprayed with gold.

2.3. Experiments

An adsorption–desorption experimental device was established in order to investigate the effects of temperature, humidity and CO_2 concentration in an air-conditioned environment on the co-sorption performance of H_2O and CO_2. In addition, the stability characteristics of the adsorption–desorption cycle of three MIL adsorbent materials were also investigated.

The schematic diagram of the adsorption–desorption experimental device is shown in Fig. 1 and a photograph of the experimental device is shown in Fig. 2. The experimental device consists of a simulated gas generator, a heater, a fixed adsorption bed and a measurement and control system. The simulated gas generator is comprised of gas cylinders and a water vapor generator. The simulated gas generator is designed to provide the gas mixture required for the experiments with N_2 as the carrier gas. The water vapor is generated by a water heater with a thermostat. The heater is used to control the temperature of the mixed air. The fixed bed reactor is cylindrical with quartz sand at both ends and adsorbent material in the middle. The measurement and control system controls the flow rate of each gas path as well as the testing and controlling of the air pressure, air temperature, air humidity, and air CO_2 concentration of the incoming and outgoing fixed adsorption bed. The sample is degassed for 2 hours at a temperature of 100 °C and a flow rate of 10 mL min^{-1} of N_2. The outlet concentration was detected using a humidity sensor and a carbon dioxide sensor,
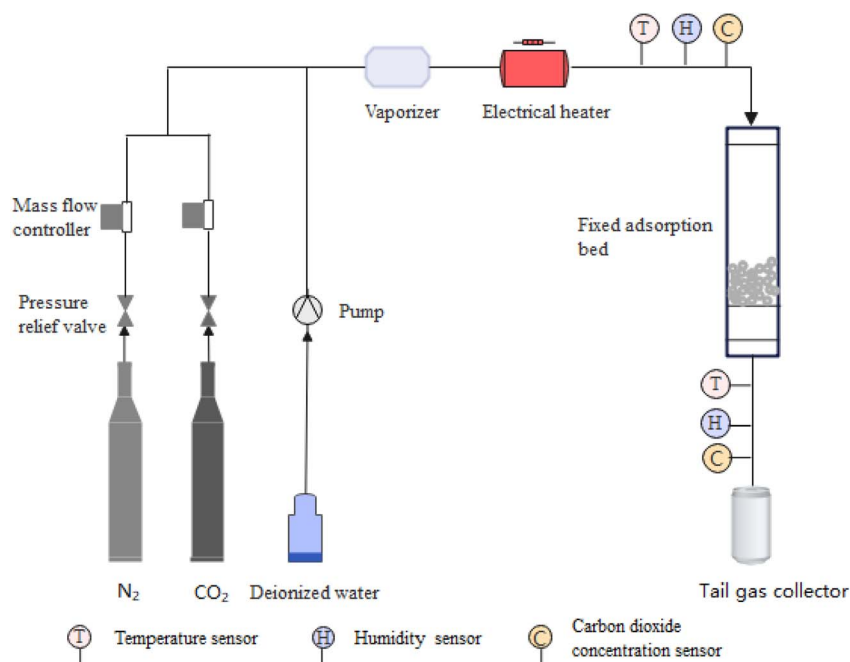

Fig. 1 Schematic diagram of the adsorption–desorption experimental device.

Fig. 2 Photograph of the adsorption–desorption experimental device.

and degassing is deemed complete when there is no longer any detectable water vapor or carbon dioxide. Degassing temperature 100 °C is determined based on the regeneration temperature obtained from a study of three MOF materials in in SAACs.[13,37] Before adsorption, N_2 is heated to 80 °C and the pipeline is purged for 0.5 hours to get rid of any remaining gases and moisture. The samples are tested three times in parallel using 4 g of the adsorbent material in each experiment, and the test results are used as the evaluation value. The air-conditioned environment is at atmospheric pressure, so the experiments are conducted at atmospheric pressure. Pressure sensors, temperature sensors, humidity sensors and CO_2 concentration sensors were used to collect and record the experimental data *via* a computer. The measurement parameters used for the experimental device as well as the type and accuracy of the sensor are shown in Table 1. The sensor locations are illustrated in Fig. 1.

2.4. Performance index

2.4.1 Isoteric heat of adsorption.
Isoteric heat of adsorption can be calculated using the following equation:[38]

$$\ln P_v = -\frac{\Delta H}{RT} + K \tag{1}$$

where ΔH is the isoteric heat of adsorption (kJ mol^{-1}); P_v is the vapor partial pressure (Pa); R is the molar gas constant, kJ mol^{-1} °C^{-1}; T is the temperature (K); K is the integral constant.

2.4.2 Saturation dehumidification capacity (W).
Saturation dehumidification capacity (W) is calculated as follows:

$$W = \frac{M_{H_2O}fC_{1,W}}{m}\int_0^{\tau_W}\left(1 - \frac{C_{2,W}}{C_{1,W}}\right)d\tau$$
$$= \frac{M_{H_2O}f}{m}\left(C_{1,W}\tau_W - \int_0^{\tau_W}C_{2,W}d\tau\right) \tag{2}$$

where W is the saturation dehumidification capacity, mg g^{-1}; M_{H_2O} is the molar mass of water, 18 g mol^{-1}; f is inlet gas flow rate, L s^{-1}; $C_{1,W}$ and $C_{2,W}$ are the inlet and outlet H_2O concentration, mmol L^{-1}; m is the adsorbent material mass, g; τ_W is the saturation dehumidification breakthrough time, s, τ_W is the time when the outlet H_2O concentration is 95% of the inlet H_2O concentration.

The relationship between H_2O concentration and relative humidity is as follows:

$$C_W = \frac{0.0415\varphi P_s}{P - \varphi P_s} \tag{3}$$

where C_W is H_2O concentration, mmol L^{-1}; φ is relative humidity%; P_s is saturated vapor pressure of water vapor, Pa; P is atmospheric pressure, Pa.

2.4.3 Saturation decarburization capacity (C).
Saturation decarburization capacity (C) is calculated as follows:

$$C = \frac{M_{CO_2}fC_{1,C}}{m}\int_0^{\tau_C}\left(1 - \frac{C_{2,C}}{C_{1,C}}\right)d\tau$$
$$= \frac{M_{CO_2}f}{m}\left(C_{1,C}\tau_C - \int_0^{\tau_C}C_{2,C}d\tau\right) \tag{4}$$

where C is the saturation carbon removal capacity, mg g^{-1}; M_{CO_2} is the molar mass of CO_2, 44 g mol^{-1}; $C_{1,C}$ and $C_{2,C}$ are the inlet and outlet CO_2 concentration, mmol L^{-1}; τ_W is the saturation decarburization breakthrough time, s, τ_W is the time when the outlet CO_2 concentration is 95% of the inlet CO_2 concentration.

2.4.4 Air conditioning dehumidification capacity (AW).
When the H_2O concentration reaches 0.493 mmol L^{-1}, the dehumidification capacity meets the air supply requirements of the air-conditioned room.[39,40] The corresponding breakthrough time and adsorption volume are the air conditioning dehumidification breakthrough time and the air conditioning dehumidification capacity. When the outlet H_2O concentration reaches 0.493 mmol L^{-1}, the corresponding breakthrough time is τ_{AW}, AW is calculated as follows:

Table 1 The parameters of the measuring instrument

Measuring instrument	Specification model	Measuring range	Measuring accuracy
Pressure sensors	MIK-P300	−0.1 Mpa–60 Mpa	±1%
Temperature sensors	PT100	−40 °C–100 °C	±0.15 °C
Humidity sensor	TH800ST5	0–100%	±2%
CO_2 sensor	RS-CO2WS-N01	0 ppm–10 000 ppm	±(50 ppm + 3% F.S)
Gas flow meter	AMS2106	0 mL min^{-1}–200 mL min^{-1}	±3% F.S

$$AW = \frac{M_{H_2O}fC_{1,W}}{m} \int_0^{\tau_{AW}} \left(1 - \frac{C_{2,AW}}{C_{1,W}}\right)d\tau$$

$$= \frac{M_{H_2O}f}{m} \left(C_{1,W}\tau_{AW} - \int_0^{\tau_{AW}} C_{2,AW}d\tau\right) \quad (5)$$

2.4.5 Air conditioning decarburization capacity (AC). When the outlet CO_2 concentration is 0.1%, the decarburization capacity meets the air supply requirements of the air-conditioned room.[39,40] The corresponding breakthrough time and adsorption volume are the air conditioning decarburization breakthrough time and the air conditioning decarburization capacity. When the outlet air CO_2 concentration reaches 0.1%, the corresponding breakthrough time is τ_{AC}, AC is calculated as follows:

$$AC = \frac{M_{CO_2}fC_{1,C}}{m} \int_0^{\tau_{AC}} \left(1 - \frac{C_{2,AC}}{C_{1,C}}\right)d\tau$$

$$= \frac{M_{CO_2}f}{m} \left(C_{1,C}\tau_{AC} - \int_0^{\tau_{AC}} C_{2,AC}d\tau\right) \quad (6)$$

3. Results and discussion

3.1. Characterization of three MIL adsorbent materials

3.1.1 Pore structure analysis. The pore structure parameters of the three MOFs adsorbent materials and the silica gel are listed in Table 2, with MIL-101(Cr) having the largest specific surface area and total pore volume, followed by MIL-101(Fe), MIL-100 (Fe) is smaller and SG is the smallest. For comparison, the pore structure parameters of the three MOFs adsorbent materials synthesized by hydrothermal or solvent thermal method reported in other literatures are listed in Table 2.

From the data in the table, it can be seen that the BET surface area and pore volume of MIL-101(Cr) and MIL-101(Fe) obtained in this paper are similar to those reported in the literature. The BET surface area and pore volume of MIL-100(Fe) obtained in this work are meaningful different from those reported in the literature, which may be caused by the difference in the respective synthesis and purification methods used, especially for the solvent concentration.[41]

3.1.2 PXRD analysis. Fig. 3 depicts the powder X-ray diffraction (PXRD) patterns of the three MOF adsorbent

Table 2 Pore structure parameters of adsorbent materials

Adsorption materials	BET surface area ($m^2\ g^{-1}$)	Pore volume ($cm^3\ g^{-1}$)	Ref.
MIL-101(Cr)	2831	1.54	This work
MIL-101(Cr)	3017	1.61	21
MIL-101(Cr)	2578	1.25	42
MIL-101(Fe)	2308	1.23	This work
MIL-101(Fe)	1413	0.75	43
MIL-101(Fe)	2350	1.36	44
MIL-100(Fe)	1089	0.43	This work
MIL-100(Fe)	1917	1.00	45
MIL-100(Fe)	1549	0.82	46
SG	312	0.22	This work
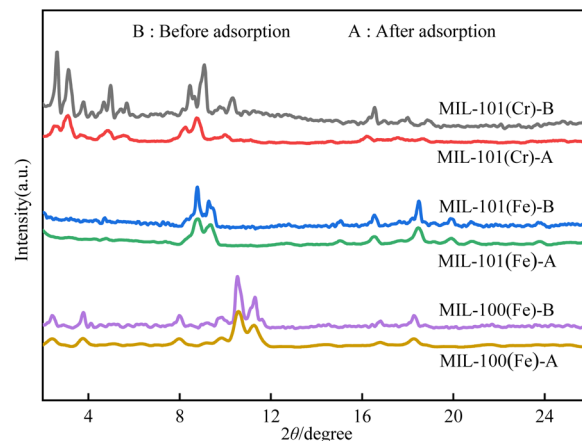
(a) MIL-101(Cr), MIL-101(Fe) and MIL-100(Fe)
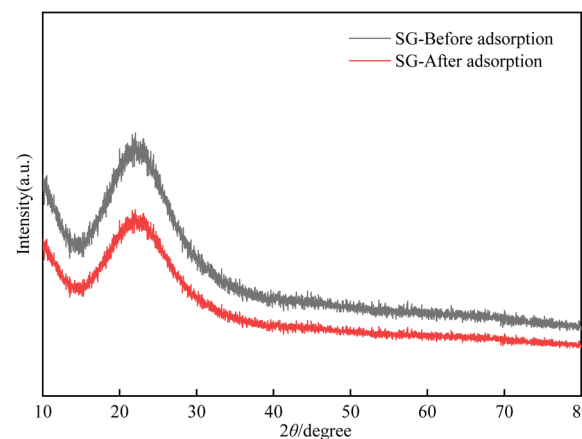
(b) SG

Fig. 3 Powder X-ray diffraction patterns of the adsorbent materials: (a) MIL-101(Cr), MIL-101(Fe) and MIL-100(Fe), (b) SG.

materials and silica gel before and after adsorption (SG). Adsorption conditions: temperature 303 K, relative humidity 50%, CO_2 concentration 0.3%. The PXRD patterns of the adsorbed materials before and after adsorption are essentially the same, as shown in Fig. 3. It means that there was no chemical reaction before or after adsorption. According to the literature,[47] the two distinct characteristic peaks of MIL-101(Cr) are located at 8.4° and 9.2°, as shown in Fig. 3a. MIL-101(Fe) has distinct characteristic peaks of 8.8°, 16.5°, and 18.6°, which are consistent with the literature results.[48] The characteristic peaks of MIL-100(Fe) are 10.5° and 11.3°, which are in accordance with the findings of the literature.[49] The results indicate that the prepared the three MIL adsorbent materials have a high purity. Combined with the scanning electron microscopy (SEM) photographs, it was determined that the three MOF adsorbent materials were good crystallinity. The PXRD pattern of the silica gel is shown in Fig. 3b. It can be seen from Fig. 3b that a relatively significant amorphous silica peak package appears in the PXRD spectrum, indicating that the prepared silica gel sample is composed of amorphous silica. In addition, no other sharp crystal diffraction peaks are found in the spectrum.
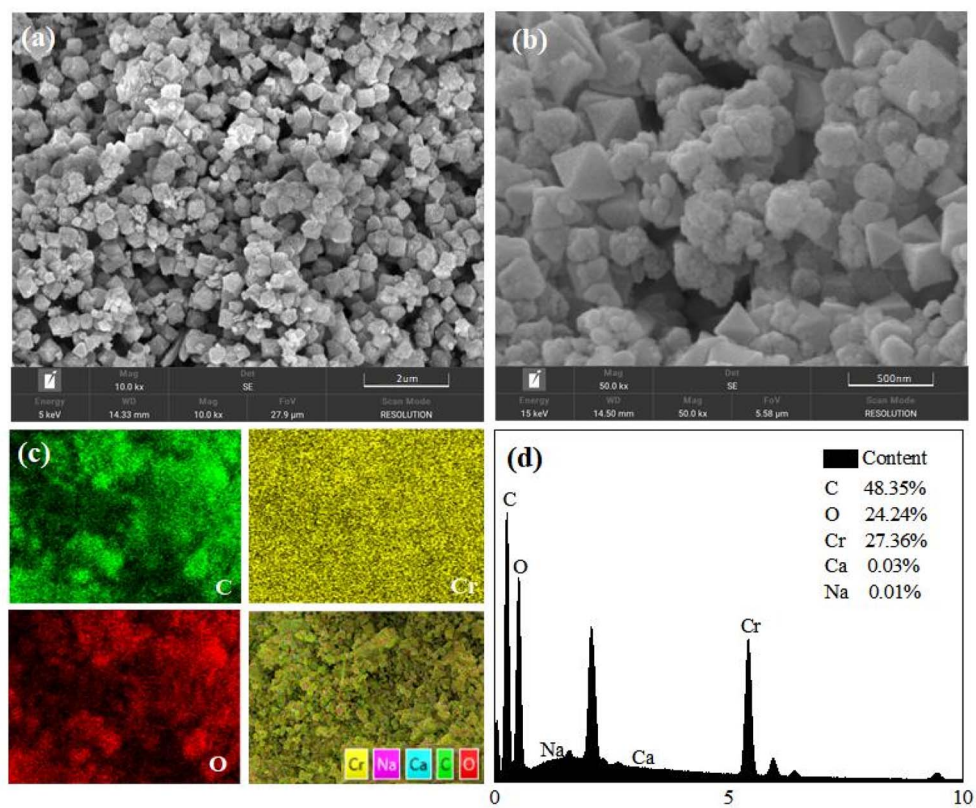
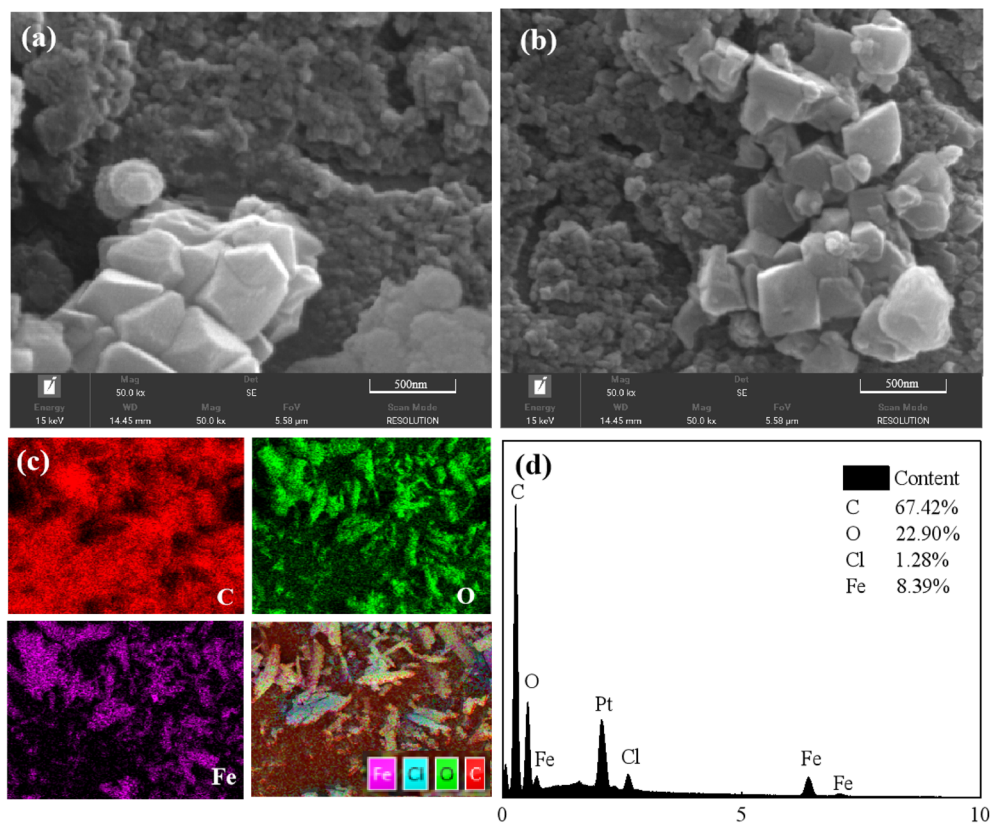Fig. 4 SEM image and EDS analysis of MIL-101(Cr).

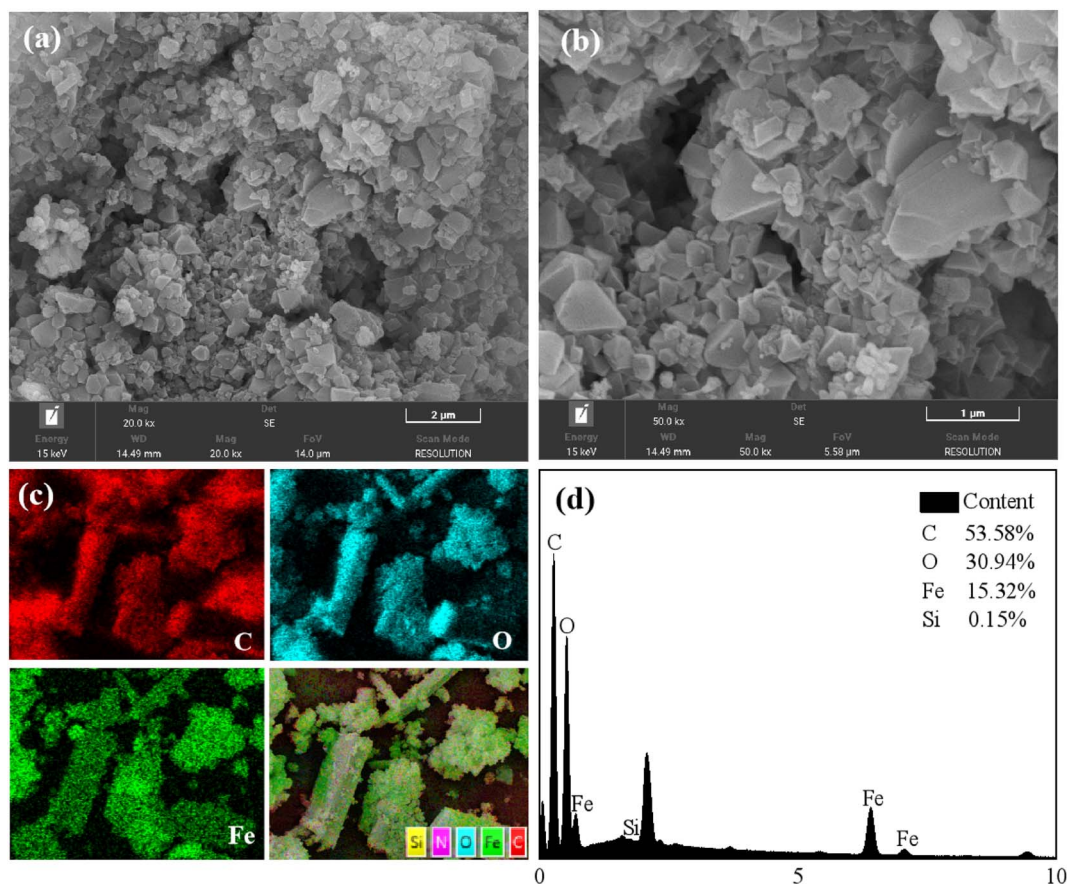Fig. 5 SEM image and EDS analysis of MIL-101(Fe).

Fig. 6 SEM image and EDS analysis of MIL-100(Fe).

3.1.3 SEM-EDS analysis. The surface morphology, crystallization and composition of the adsorbent material were analyzed by SEM and EDS. As shown in Fig. 4, MIL-101(Cr) is an octahedral material with uniform particle size and contains C, O and Cr elements with 49.35%, 24.24% and 27.36% by mass, respectively, with morphology and composition approximating those of the literature.[50] As shown in Fig. 5, MIL-101(Fe) is a regular octahedron and contains C, O, Cl and Fe elements with 67.42%, 22.90%, 1.28% and 8.39% by mass, respectively, with morphology and composition approximating those of the literature.[35] As seen in Fig. 6, MIL-100(Fe) is a typical octahedral structure and contains C, O and Fe elements in amounts of 53.58%, 30.94% and 15.32% by mass, respectively, with approximates the morphology and composition of the literature (Fig. 7).[35]

3.2. Isosteric heat of adsorption of H_2O on the three MIL adsorbent materials

The isosteric heat of adsorption of H_2O on the three MIL adsorbent materials were calculated for a binary gas (H_2O/N_2) with N_2 as carrier gas and a relative humidity of 80% and the isosteric heat of adsorption of a ternary gas ($H_2O/N_2/CO_2$) with N_2 as carrier gas and a relative humidity of 80% and a CO_2 concentration of 0.3%. Fig. 8 illustrates the isosteric heat of adsorption of H_2O on the three MIL adsorbent materials. It can

be seen from Fig. 8 that the ΔH H_2O on three MIL adsorbent materials decreases with an increase in the W. This is due to in the dehumidification process, the strong adsorption sites are occupied, the dehumidification capacity of the three adsorption materials is gradually consumed. The magnitude of the isosteric heat of adsorption of H_2O for the three MIL adsorbent materials is: ΔH (MIL-101(Cr)) > ΔH (MIL-101(Fe)) > ΔH (MIL-100(Fe)). At surface coverage 100–200 mg g^{-1}, the isosteric heat of adsorption of H_2O on silica gel was 27.1–29.3 kJ mol^{-1}. All three MIL adsorbent materials had higher isosteric heats of adsorption than silica gel.

The interaction of H_2O with the adsorbent materials is stronger in the binary gas mixtures compared to the ternary gas mixtures. At low surface coverage ($W = 108$ mg g^{-1}), the isosteric heats of adsorption of t MIL-101(Cr), MIL-101(Fe) and MIL-100(Fe) in the binary gas mixtures were 50 kJ mol^{-1}, 39 kJ mol^{-1} and 35 kJ mol^{-1}, compared with the ternary gas mixtures, which increased by 4.0%, 5.1% and 8.6%. At medium surface coverage ($W = 324$ mg g^{-1}), the isosteric heats of adsorption of MIL-101(Cr), MIL-101(Fe) and MIL-100(Fe) in the binary gas mixtures were 47 kJ mol^{-1}, 37 kJ mol^{-1} and 23 kJ mol^{-1}, compared with the ternary gas mixtures, which increased by 4.3%, 5.4% and 8.7%. At high surface coverage ($W = 540$ mg g^{-1}), the isosteric heats of adsorption of MIL-101(Cr), MIL-101(Fe) and MIL-100(Fe) in the binary gas mixtures were
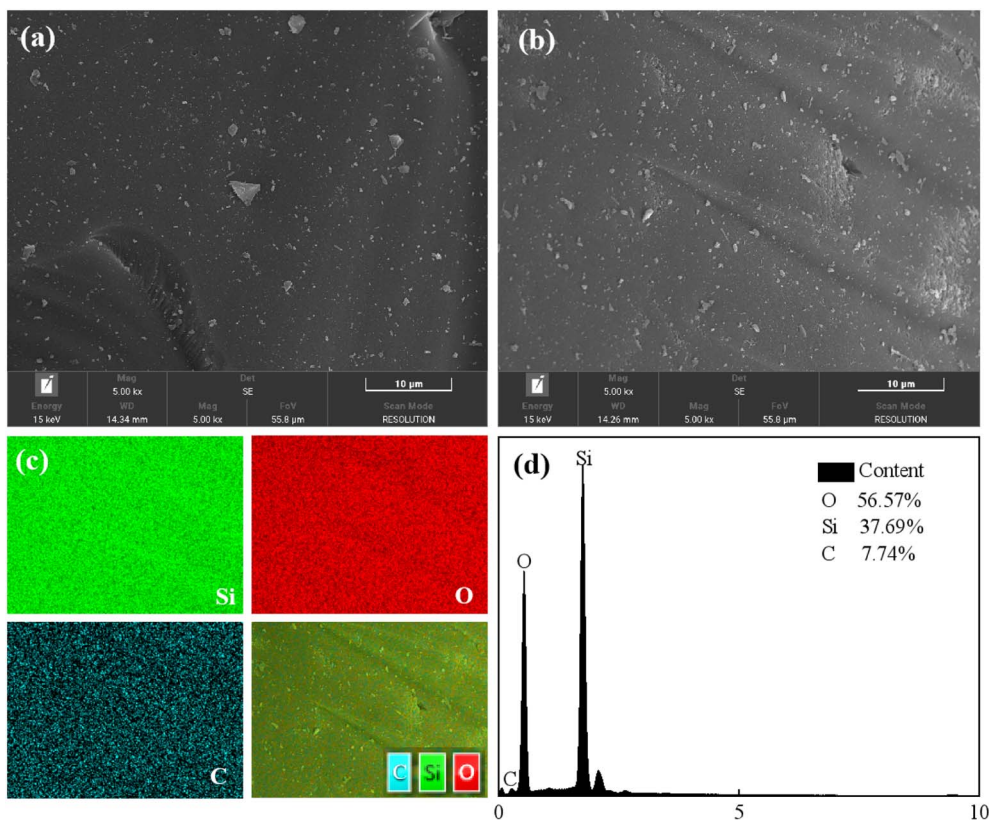
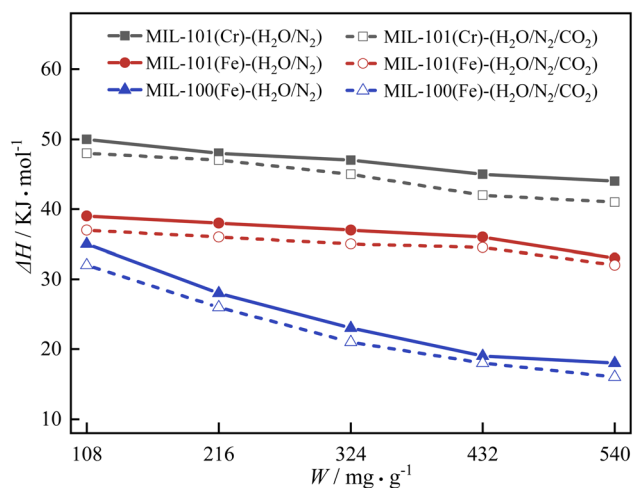**Fig. 7** SEM image and EDS analysis of SG.

Fig. 8 Isosteric heat of adsorption H_2O on the three MIL adsorbent materials.

44 kJ mol^{-1}, 33 kJ mol^{-1} and 18 kJ mol^{-1}, compared with the ternary gas mixtures, which increased by 6.8%, 3.0% and 11.1%.
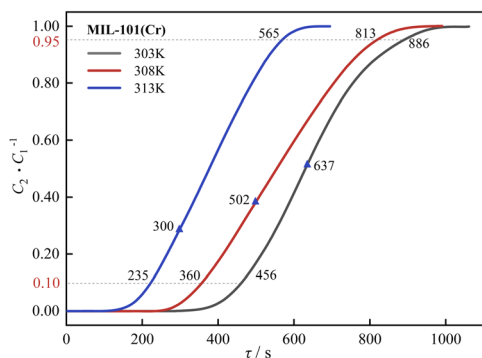
3.3. Dehumidification and decarburization performance

The temperature, humidity and CO_2 concentration in SAACs vary within a certain range depending on the outdoor meteorological parameters and the personnel in the room. Therefore, it is important to investigate the effects of temperature,

humidity and CO_2 concentration on the dehumidification and decarburization performance of adsorbent materials. The dehumidification and decarburization performance of the conventional dehumidification material silica gel (SG) was also tested for comparison purposes. The breakthrough curves of three MIL adsorbent materials for H_2O and CO_2 were tested at different temperatures, humidity and CO_2 concentrations for ternary gas ($H_2O/N_2/CO_2$) with N_2 as the carrier gas at atmospheric pressure and an inlet gas flow rate of 65 mL min^{-1}. The outlet concentration of 10% and 95% of the inlet concentration are set as the breakthrough and saturation points, the outlet H_2O concentration of 0.493 mmol L^{-1} is set as the air conditioning dehumidification point, and an outlet CO_2 concentration of 0.1% is set as the air conditioning decarburization point.

3.3.1 Effect of temperature on dehumidification and decarburization performance. The effect of temperature on the dehumidification and decarburization performance of three MIL adsorbent materials and SG were investigated at a relative humidity of 50% and a CO_2 concentration of 0.3%. The breakthrough curves of adsorption (dehumidification and decarburization) are shown in Fig. 9 and 10. The saturation dehumidification capacity and saturation decarburization capacity and air conditioning dehumidification capacity and air conditioning decarburization capacity are shown in Fig. 11 and 12.

As shown in Fig. 9 and 10, the breakthrough time, saturation time and air conditioning time of three MIL adsorbent
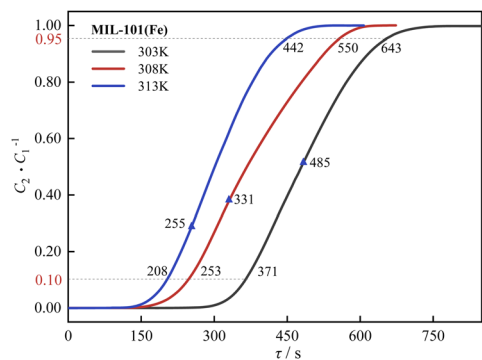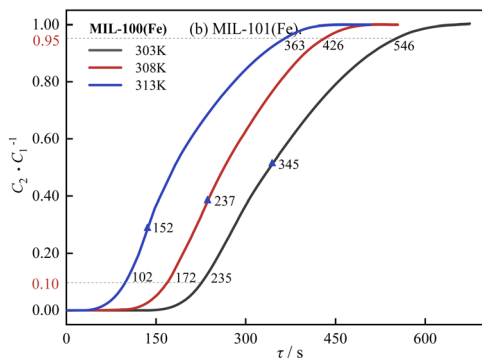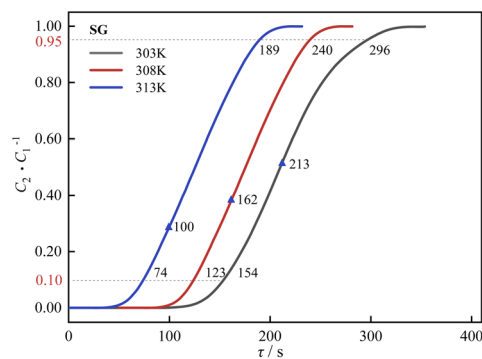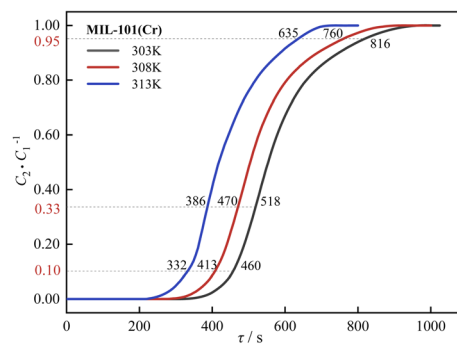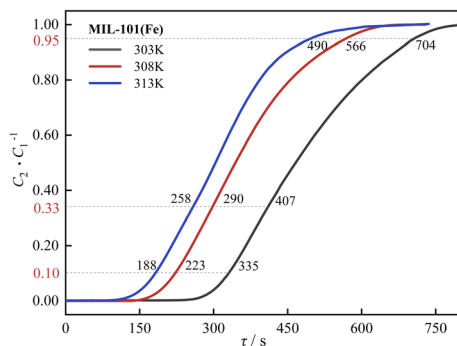
Fig. 9 Effect of temperature on dehumidification performance: (a) MIL-101(Cr), (b) MIL-101(Fe), (c) MIL-100(Fe), (d) SG.
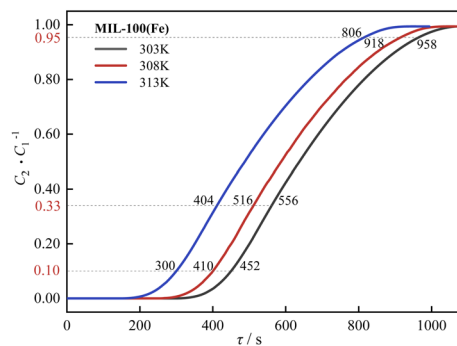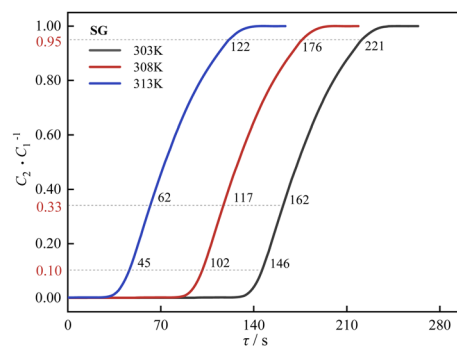

Fig. 10 Effect of temperature on decarburization performance: (a) MIL-101(Cr), (b) MIL-101(Fe), (c) MIL-100(Fe), (d) SG.

materials and SG for H_2O and CO_2 decreased gradually as the temperature rose from 303 K to 313 K. This is because the adsorption reaction of three MIL adsorbent materials and SG

are exothermic, and the adsorption reaction is inhibited by high temperatures, resulting in a decrease in the adsorption capacity.[51]
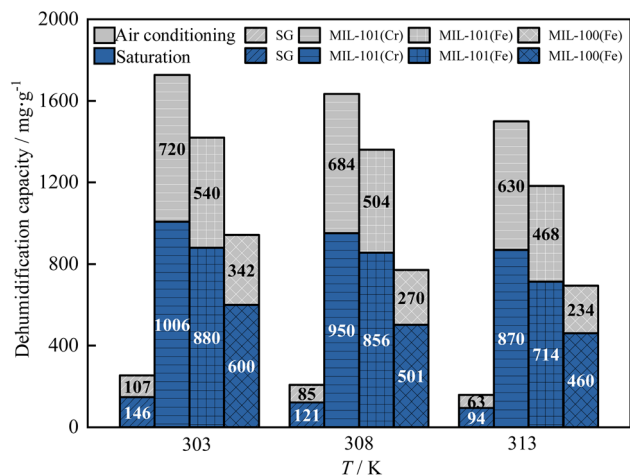
Fig. 11 Effect of temperature on dehumidification capacity.
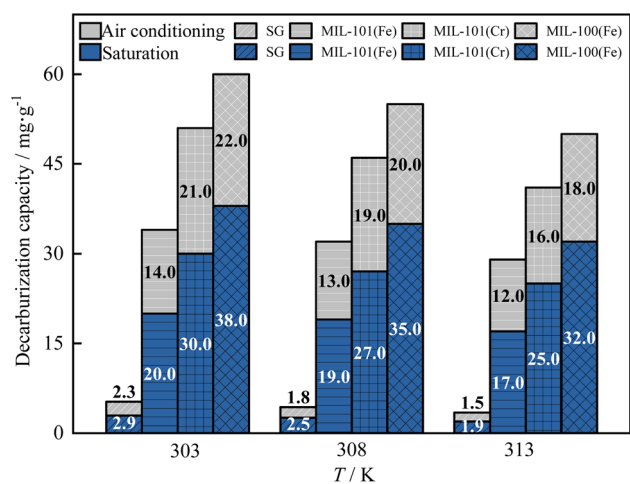
Fig. 12 Effect of temperature on decarburization capacity.

As shown in Fig. 11, as the temperature rose from 303 K to 313 K, the saturation dehumidification capacity and the air conditioning dehumidification capacity of MIL-101(Cr) decreased by 13.5% and 12.5%, respectively. The saturation dehumidification capacity and the air conditioning dehumidification capacity of MIL-101(Fe) decreased by 18.9% and 13.3%. The saturation dehumidification capacity and the air conditioning dehumidification capacity of MIL-100(Fe) decreased by 23.3% and 31.6%. MIL-100(Fe) showed the largest drop in dehumidification capacity, indicating that the dehumidification capacity of the MIL-100(Fe) was most affected by temperature.

As shown in Fig. 12, as the temperature rose from 303 K to 313 K, the saturation decarburization capacity and the air conditioning decarburization capacity of MIL-101(Cr) decreased by 16.7% and 23.8%. The saturation decarburization capacity and the air conditioning decarburization capacity of MIL-101(Fe) decreased by 15.0% and 14.3%. The saturation decarburization capacity and the air conditioning decarburization capacity of MIL-100(Fe) decreased by 15.8% and 18.2%. The

decarburization capacity of MIL-101(Cr) decreased the most, indicating that the decarburization capacity of MIL-101(Cr) was most affected by temperature.

The dehumidification capacity of three MIL adsorbent materials and SG followed the sequence of MIL-101(Cr) > MIL-101(Fe) > MIL-100(Fe) > SG. The decarburization capacity of three MIL adsorbent materials and SG followed the sequence of MIL-100(Fe) > MIL-101(Cr) > MIL-101(Fe) > SG. At 303 K, the dehumidification capacity of MIL-101(Cr) is 6.9 times that of SG and the decarburization capacity of MIL-101(Cr) is 13.1 times that of SG.

In summary, the temperature has a significant effect on dehumidification and decarburization performance of three MIL adsorbent materials and SG, with MIL-100(Fe) having the greatest effect on dehumidification and MIL-101(Cr) having the greatest effect on decarburization. In practice, the adsorption can be carried out by pre-cooling, which can increase both dehumidification and decarburization capacity.
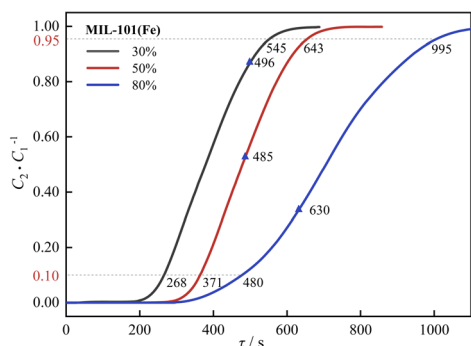
3.3.2 Effect of humidity on dehumidification and decarburization performance. The effect of relative humidity on the dehumidification and decarburization performance of three MIL adsorbent materials and SG were investigated at a temperature of 303 K and a CO_2 concentration of 0.3%. The breakthrough curves of adsorption (dehumidification and decarburization) are shown in Fig. 13 and 14. The saturation dehumidification capacity and saturation decarburization capacity and air conditioning dehumidification capacity and air conditioning decarburization capacity are shown in Fig. 15 and 16.

As shown in Fig. 13 and 14, as the relative humidity increased from 30% to 80%, the breakthrough dehumidification time, saturation dehumidification time and air conditioning dehumidification time of the three MIL adsorbent materials and SG increased, the breakthrough decarburization time, saturation decarburization time, air conditioning decarburization time decreased gradually for MIL-101(Cr) and MIL-101(Fe), and the breakthrough decarburization time, saturation decarburization time, air conditioning decarburization time increased first and then decreased for MIL-100(Fe), reaching a maximum at a relative humidity of 50%.

As shown in Fig. 15 and 16, as the relative humidity increased from 30% to 80%, the saturation dehumidification capacity and air conditioning dehumidification capacity of MIL-101(Cr) increased by 36.8% and 12.4%, and the saturation decarburization capacity and air conditioning decarburization capacity of MIL-101(Cr) decreased by 50.0% and 54.5%. As the relative humidity increased from 30% to 80%, the saturated dehumidification capacity and air conditioning dehumidification capacity of MIL-101(Fe) increased by 69.3% and 27.1%, and the saturated decarburization capacity and air conditioning decarburization capacity of MIL-101(Fe) decreased by 51.2% and 34.6%. The BET surface area of three MIL adsorbent materials after adsorption at high humidity were tested. The results showed that compared to the BET surface area before adsorption, the BET surface area of MIL-101(Cr) after adsorption decreased from 2831 $m^2 g^{-1}$ to 2503 $m^2 g^{-1}$, the BET surface area of MIL-101 (Fe) decreased from 2308 $m^2 g^{-1}$ to 2106
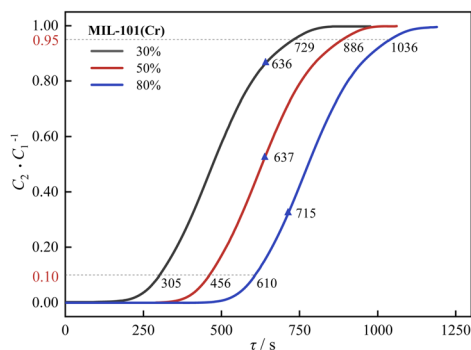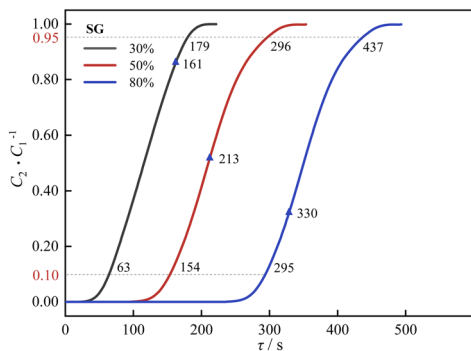
(a) MIL-101(Cr).

(b) MIL-101(Fe).
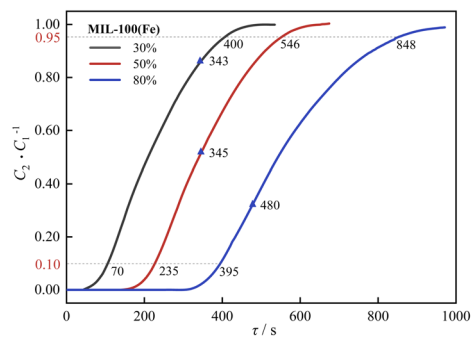
(c) MIL-100(Fe).

(d) SG

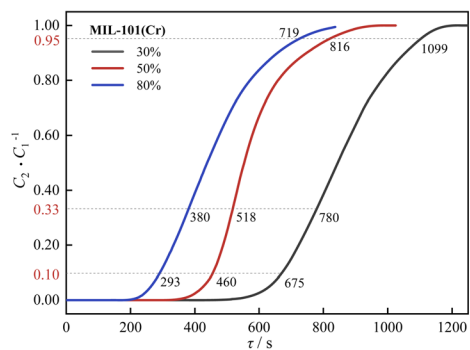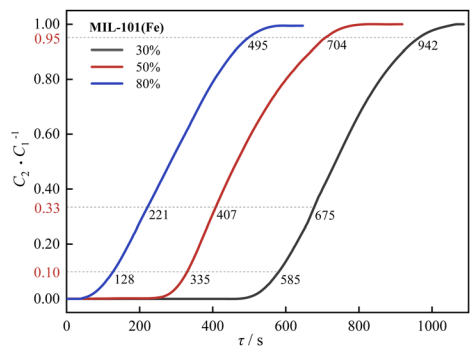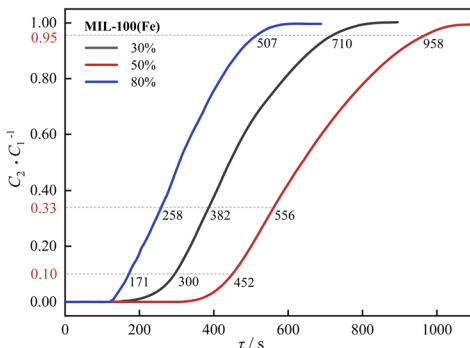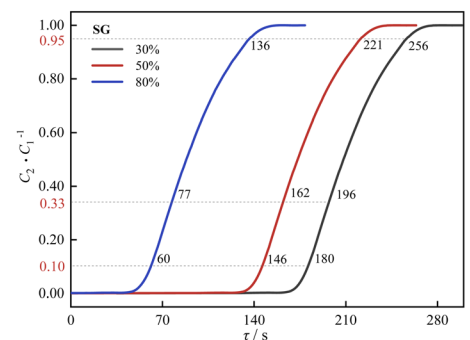**Fig. 13** Effect of humidity on dehumidification performance: (a) MIL-101(Cr), (b) MIL-101(Fe), (c) MIL-100(Fe), (d) SG.

(a) MIL-101(Cr).

(b) MIL-101(Fe).

(c) MIL-100(Fe).

(d) SG

Fig. 14 Effect of humidity on decarburization performance: (a) MIL-101(Cr), (b) MIL-101(Fe), (c) MIL-100(Fe), (d) SG.

$m^2\ g^{-1}$, and the BET surface area of MIL-100 (Fe) decreased from 1089 $m^2\ g^{-1}$ to 970 $m^2\ g^{-1}$. This further indicates that H_2O occupies the pore channels of MIL-101(Cr) and MIL-101(Fe) at

high humidity, reducing the amount of CO_2 adsorbed by MIL-101(Cr) and MIL-101(Fe).[32] As the relative humidity increased from 30% to 80%, the saturation dehumidification capacity and
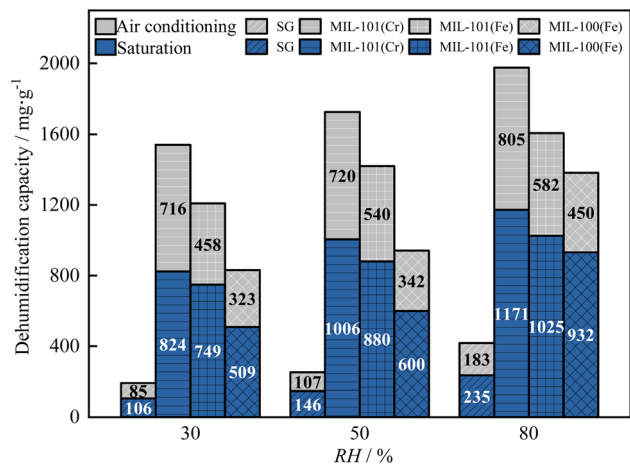
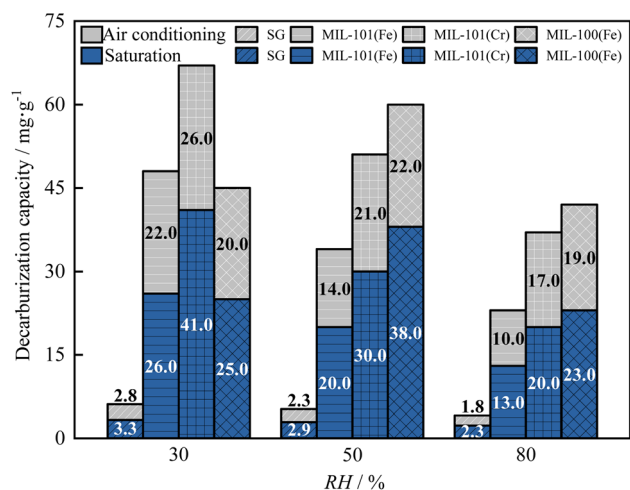Fig. 15 Effect of humidity on dehumidification capacity.

Fig. 16 Effect of humidity on decarburization capacity.

air conditioning dehumidification capacity of MIL-100(Fe) increased by 83.1% and 39.3%. As the relative humidity increased from 30% to 80%, the saturation decarburization capacity and air conditioning decarburization capacity of MIL-100(Fe) increased by 52.0% and 10.0%. This is due to the fact that at higher humidity (50%), water vapor combined with MIL-100(Fe) undergoes hydrolysis, forming new alkaline adsorption sites and improving the adsorption performance of MIL-

100(Fe).[52] With an increase in relative humidity from 50% to 80%, the saturation decarburization capacity and air conditioning decarburization capacity by MIL-100(Fe) decreased by 39.5% and 13.6%. This is because at high humidity (80%), water vapor causes collapse of some of the pore channels of MIL-100(Fe), reducing the carbon removal performance of MIL-100(Fe).

Air conditioning dehumidification capacity of three MIL adsorbent materials and SG: MIL-101(Cr) > MIL-101(Fe) > MIL-100(Fe)> SG. Air conditioning decarburization capacity of three MIL adsorbent materials and SG: low humidity: MIL-101(Fe) > MIL-101(Cr) > MIL-100(Fe) > SG, medium and high humidity: MIL-100(Fe) > MIL-101(Fe) > MIL-101(Cr) > SG.

The available literature mostly focuses on dehumidification using MIL-101(Cr) and MIL-100(Fe), but MIL-101(Fe) was primarily used at much higher CO_2 concentrations than in this work and is therefore not comparable. Table 3 compares MIL-101(Cr) and MIL-100(Fe) used in this work with MIL-101(Cr) and MIL-100(Fe) from the literature in terms of saturation dehumidification capacity. When comparing the temperature and humidity in the literature, the temperature and humidity in this work were essentially close, and the higher dehumidification capacity was caused by the lower temperature in the comparative literature. Compared with the dehumidification capacity, the dehumidification capacity in this work are basically in line with the literature, indicating that the effect of CO_2 on the dehumidification capacity is small, suggesting that MIL-101(Cr) and MIL-100(Fe) can achieve better co-adsorption of H_2O and CO_2.

3.3.3 **Effect of CO_2 concentration on dehumidification and decarburization performance.** The effect of CO_2 concentration on the dehumidification and decarburization performance of three MIL adsorbent materials and SG were investigated at a temperature of 303 K and a relative humidity of 50% (corresponding to a H_2O concentration of 0.930 mmol L^{-1}). The breakthrough curves of adsorption (dehumidification and decarburization) are shown in Fig. 17 and 18. The saturation dehumidification capacity and saturation decarburization capacity and air conditioning dehumidification capacity and air conditioning decarburization capacity are shown in Fig. 19 and 20.
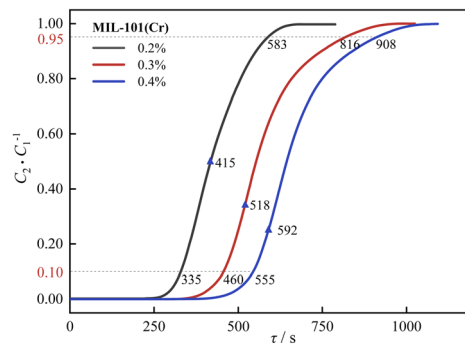
As shown in Fig. 17, the breakthrough dehumidification time, saturation dehumidification time and air conditioning dehumidification time decreased for three MIL adsorbent materials and SG as the CO_2 concentration increased. As shown in Fig. 18, the breakthrough decarburization time, saturation

Table 3 Dehumidification capacity comparison of MIL–101(Cr) and MIL–100(Fe)
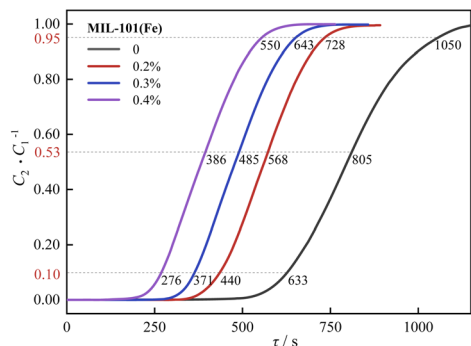
Adsorption materials	Temperature (K)	Relative humidity (%)	Dehumidification capacity (g mg^{-1})	Ref.
MIL-101(Cr)	298	50	916	53
MIL-101(Cr)	293	60	900	54
MIL-101(Cr)	293	60	1080	34
MIL-100(Fe)	288	60	690	55
MIL-101(Cr)	303	50	1006	This work
MIL-100(Fe)	303	50	600	This work
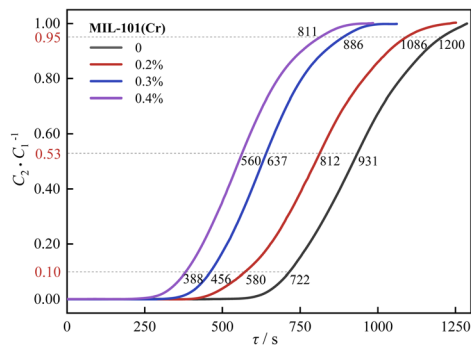
(a) MIL-101(Cr).
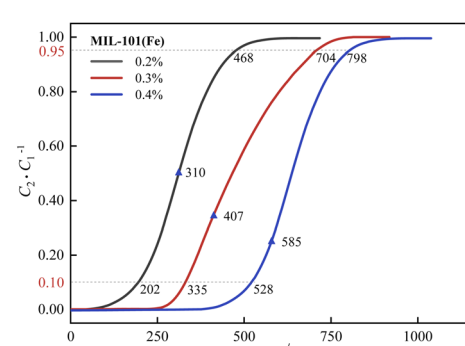
(b) MIL-101(Fe).

(c) MIL-100(Fe).

(d) SG

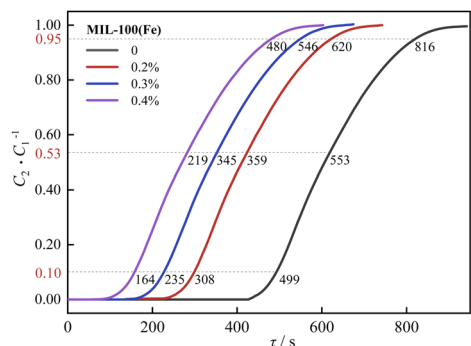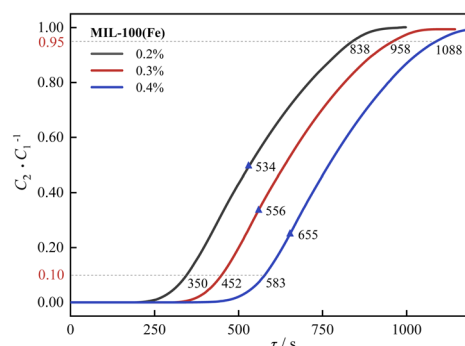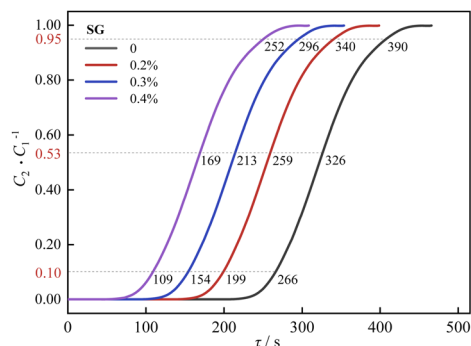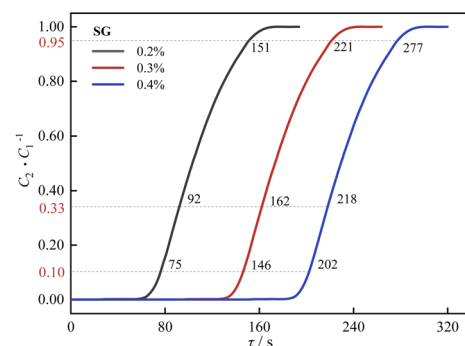**Fig. 17** Effect of CO_2 concentration on dehumidification performance: (a) MIL-101(Cr), (b) MIL-101(Fe), (c) MIL-100(Fe), (d) SG.

(a) MIL-101(Cr).

(b) MIL-101(Fe).

(c) MIL-100(Fe).

(d) SG

Fig. 18 Effect of CO_2 concentration on decarburization performance: (a) MIL-101(Cr), (b) MIL-101(Fe), (c) MIL-100(Fe), (d) SG.

decarburization time and air conditioning decarburization time increased with increasing CO_2 concentration for three MIL adsorbent materials and SG.

As shown in Fig. 19, saturation dehumidification capacity and air conditioning dehumidification capacity of MIL-101(Cr) decreased by 32.4% and 52.0% when the CO_2 concentration
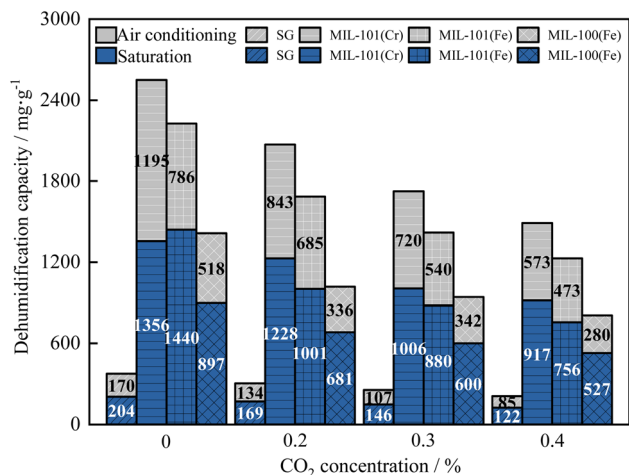
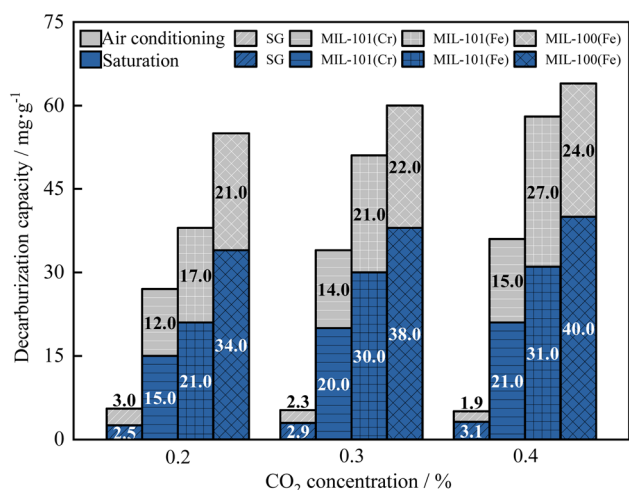Fig. 19 Effect of CO_2 concentration on dehumidification capacity.

Fig. 20 Effect of CO_2 concentration on decarburization capacity.

As a result, CO_2 inhibits the adsorption rate and capacity of the adsorbent materials for H_2O. Even at high CO_2 concentrations, three metal–organic framework materials can meet the co-adsorption requirements of dehumidification and decarburization for air conditioning. When the CO_2 concentration is 0.4%, the air conditioning dehumidification of MIL-101(Fe) is 5.6 times that of SG, and the air conditioning decarburization is 14.2 times that of SG. In practice, MIL-101(Fe) is recommended for solid adsorption air conditioning at high CO_2 concentrations due to its high co-adsorption capacity for both H_2O and CO_2 at high CO_2 concentrations.

3.4. Multiple adsorption–desorption cycles

Adsorption–desorption cycle characteristics are one of the most critical parameters in evaluating the performance of an adsorbent material.

Fig. 21 shows six continuous adsorption–desorption cycles on three MIL adsorbent materials and SG. Adsorption was at 303 K with a relative humidity of 50% and a CO_2 concentration
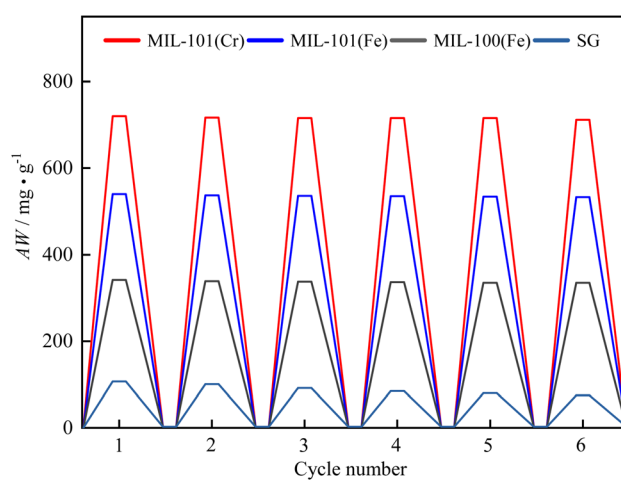
(a) H_2O
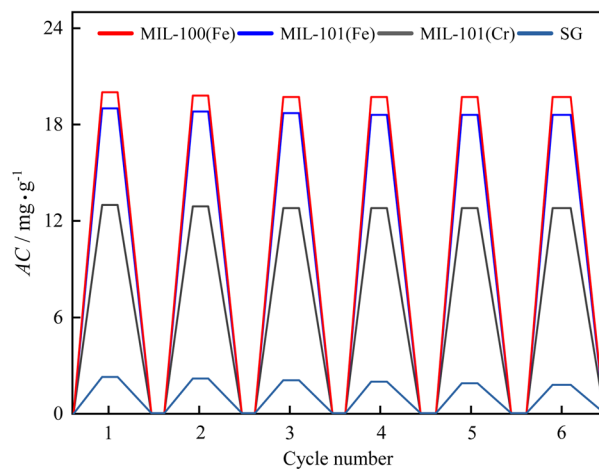
(b) CO_2

Fig. 21 Adsorption–desorption cycle characteristic: (a) H_2O, (b) CO_2.

increased from 0 to 0.4%. Saturation dehumidification capacity and air conditioning dehumidification capacity of MIL-101(Fe) decreased by 47.5% and 39.8% when the CO_2 concentration increased from 0 to 0.4%. Saturation dehumidification capacity and air conditioning dehumidification capacity of MIL-100(Fe) decreased by 41.2% and 45.0% when the CO_2 concentration increased from 0 to 0.4%. This is because the pore space of the material is occupied by CO_2 molecules in the presence of CO_2.

As shown in Fig. 20, the MIL-101(Cr) saturation decarburization capacity and air conditioning decarburization capacity increased by 40.0% and 25.0%, when the CO_2 concentration increased from 0.2% to 0.4%. The MIL-101(Fe) saturation decarburization capacity and air conditioning decarburization capacity increased by 47.6% and 58.8%, when the CO_2 concentration increased from 0.2% to 0.4%. The MIL-100(Fe) saturation decarburization capacity and air conditioning decarburization capacity increased by 17.6% and 14.3%, when the CO_2 concentration increased from 0.2% to 0.4%.

of 0.3%. Three metal–organic framework materials are reversible for H_2O and CO_2 adsorption. After six cycles of regeneration, the air conditioning dehumidification capacity of MIL-101(Cr), MIL-101(Fe), and MIL100 (Fe) decreased by 1.1%, 1.3% and 1.9%, respectively, and the air conditioning decarbonization capacity decreased by 1.5%, 1.8% and 1.3%, respectively, all within 2%. There was no significant loss of adsorption capacity of the three metal–organic framework materials. The loss of dehumidification capacity was generally consistent with the experimental findings of Seo et al.[55] After six consecutive adsorption–desorption cycles of SG, the dehumidification of air conditioning decreased by 30.0%, and the decarburization of air conditioning decreased by 21.7%. The results show that the three metal–organic framework materials have good co-adsorption reversibility for H_2O and CO_2.

4. Conclusion

Three metal–organic framework materials, MIL-101(Cr), MIL-101(Fe) and MIL-100(Fe), were successfully synthesized by the hydrothermal method. The co-adsorption performance of three MIL adsorbent materials and SG on H_2O and CO_2 was studied comparatively by building a fixed bed adsorption/desorption experimental device. Ternary gas $N_2/H_2O/CO_2$ breakthrough experiments were carried out at different temperatures, humidity and CO_2 concentrations to consider co-adsorption in different air-conditioned environments. All metal–organic framework materials can collectively adsorb H_2O and CO_2. Under high humidity conditions (at 80% relative humidity, 303 K, 0.3% CO_2 concentration), MIL-101(Cr) showed an air conditioning dehumidification capacity of up to 805 mg g^{-1}, which is 4.4 times that of SG. The MIL-100(Fe) showed an air conditioning decarburization capacity of up to 19 mg g^{-1}, which is 10.6 times that of SG. At high CO_2 concentrations (at 0.4% CO_2 concentration), 50% relative humidity, 303 K, MIL-101(Cr) shows up to 573 mg g^{-1} of air conditioning dehumidification capacity, which was 6.7 times that of SG. The MIL-101(Fe) shows up to 27 mg g^{-1} of air conditioning decarburization capacity, which was 14.2 times that of SG.

Author contributions

Liu Chen: conceptualization, methodology, and writing – review and editing; Famei Yang: data curation, formal analysis, and writing – original draft.

Conflicts of interest

The authors declare no competing interests.

Acknowledgements

References

1 Building Energy Conservation Research Center of Tsinghua University, *Research report on annual development of building energy efficiency in China*, China Architecture & Building Press, 2021.

2 B. Dai, Y. Tong, Q. Hu and Z. Chen, Characteristics of thermal stratification and its effects on HVAC energy consumption for an atrium building in south China, *Energy*, 2022, **249**, 123425, DOI: 10.1016/j.energy.2022.123425.

3 D. H. Tsai, J. S. Lin and C. C. Chan, Office workers' sick building syndrome and indoor carbon dioxide concentrations, *J. Occup. Environ. Hyg.*, 2012, **9**, 345–351, DOI: 10.1080/15459624.2012.675291.

4 K. G. Fiedoruk and D. A. Krawczyk, The possibilities of energy consumption reduction and a maintenance of indoor air quality in doctor's offices located in north-eastern Poland, *Energy Build.*, 2014, **85**, 235–245, DOI: 10.1016/j.enbuild.2014.08.041.

5 Z. J. Tu, Y. Li, S. B. Geng, K. Zhou, R. H. Wang and X. Dong, Human responses to high levels of carbon dioxide and air temperature, *Indoor Air*, 2020, **31**, 872–886, DOI: 10.1111/ina.12769.

6 T. Zhang, X. H. Liu and Y. Jiang, Development of temperature and humidity independent control (THIC) air-conditioning systems in China—A review, *Renewable Sustainable Energy Rev.*, 2014, **29**, 793–803, DOI: 10.1016/j.rser.2013.09.017.

7 W. Su, Z. F. Lu, X. H. She, J. M. Zhou, F. Wang, B. Sun and X. S. Zhang, Liquid desiccant regeneration for advanced air conditioning: A comprehensive review on desiccant materials, regenerators, systems and improvement technologies, *Appl. Energy*, 2022, **308**, 118394, DOI: 10.1016/j.apenergy.2021.118394.

8 D. C. Gao, Y. J. Sun, Z. Ma and H. Ren, A review on integration and design of desiccant air-conditioning systems for overall performance improvements, *Renewable Sustainable Energy Rev.*, 2021, **141**, 110809, DOI: 10.1016/j.rser.2021.110809.

9 D. B. Jani, M. Mishra and P. K. Sahoo, Solid desiccant air conditioning – A state of the art review, *Renewable Sustainable Energy Rev.*, 2016, **60**, 1451–1469, DOI: 10.1016/j.rser.2016.03.031.

10 A. Speerforck, J. Ling, V. Aute, R. Radermacher and G. Schmitz, Modeling and simulation of a desiccant assisted solar and geothermal air conditioning system, *Energy*, 2017, **141**, 2321–2336, DOI: 10.1016/j.energy.2017.11.151.

11 L. Chen and Y. Tan, The performance of a desiccant wheel air conditioning system with high-temperature chilled water from natural cold source, *Renewable Energy*, 2020, **146**, 2142–2157, DOI: 10.1016/j.renene.2019.08.082.

12 D. La, Y. J. Dai, Y. Li, R. Z. Wang and T. S. Ge, Technical development of rotary desiccant dehumidification and air

conditioning: A review, *Renewable Sustainable Energy Rev.*, 2010, **14**, 130–147, DOI: **10.1016/j.rser.2009.07.016**.

13 X. Zheng, T. S. Ge and R. Z. Wang, Recent progress on desiccant materials for solid desiccant cooling systems, *Energy*, 2014, **74**, 280–294, DOI: **10.1016/j.energy.2014.07.027**.

14 A. Karmakar, V. Prabakaran, D. Zhao and K. J. Chua, A review of metal-organic frameworks (MOFs) as energy-efficient desiccants for adsorption driven heat-transformation applications, *Appl. Energy*, 2020, **269**, 115070, DOI: **10.1016/j.apenergy.2020.115070**.

15 Z. Liu, C. Cheng, J. Han and X. Qi, Experimental evaluation of the dehumidification performance of a metal organic framework desiccant wheel, *Int. J. Refrig.*, 2022, **133**, 157–164, DOI: **10.1016/j.ijrefrig.2021.09.033**.

16 J. G. Lee, K. J. Bae and O. K. Kwon, Experimental investigation of the solid desiccant dehumidification system with metal organic frameworks, *Int. J. Refrig.*, 2021, **130**, 179–186, DOI: **10.1016/j.ijrefrig.2021.06.020**.

17 A. Rocchetti, M. Lippi, L. Socci, P. Gullo, V. Khorshidi and L. Talluri, Metal-Organic Framework adsorbent materials in HVAC systems: general survey and theoretical assessment, *Energies*, 2022, **15**, 8908, DOI: **10.3390/en15238908**.

18 M. Ozkan, A. A. Akhavi, W. C. Coley, R. Shang and Y. Ma, Progress in carbon dioxide capture materials for deep decarbonization, *Chem*, 2022, **8**, 141–173, DOI: **10.1016/j.chempr.2021.12.013**.

19 A. Shigematsu, T. Yamada and H. Kitagawa, Wide control of proton conductivity in porous coordination polymers, *J. Am. Chem. Soc.*, 2011, **133**, 2034–2036, DOI: **10.1021/ja109810w**.

20 J. Ehrenmann, S. K. Henninger and C. Janiak, Water adsorption characteristics of MIL-101 for heat-transformation applications of MOFs, *Eur. J. Inorg. Chem.*, 2011, **4**, 471–474, DOI: **10.1002/ejic.201001156**.

21 J. Yan, Y. Yu, C. Ma, J. Xiao, Q. Xia, Y. Li and Z. Li, Adsorption isotherms and kinetics of water vapor on novel adsorbents MIL-101(Cr)@GO with super-high capacity, *Appl. Therm. Eng.*, 2015, **84**, 118–125, DOI: **10.1016/j.applthermaleng.2015.03.040**.

22 Y. P. Yuan, H. Q. Zhang, F. Yang, N. Zhang and X. L. Cao, Inorganic composite sorbents for water vapor sorption: A research progress, *Renewable Sustainable Energy Rev.*, 2016, **54**, 761–776, DOI: **10.1016/j.rser.2015.10.069**.

23 X. Huang, Q. Hu, L. Gao, Q. Hao, P. Wang and D. Qin, Adsorption characteristics of metal–organic framework MIL-101(Cr) towards sulfamethoxazole and its persulfate oxidation regeneration, *RSC Adv.*, 2018, **8**, 27623–27630, DOI: **10.1039/C8RA04789H**.

24 E. Elsayed, A. L. Raya, S. Mahmoud, P. Anderson and A. Elsayed, Adsorption cooling system employing novel MIL-101(Cr)/CaCl$_2$ composites: numerical study, *Int. J. Refrig.*, 2019, **107**, 246–261, DOI: **10.1016/j.ijrefrig.2019.08.004**.

25 L. Chen and C. C. He, Experimental investigation of the dehumidification performance of a metal-organic framework MIL-101(Cr)/ceramic fibre paper for use as a desiccant wheel, *Microporous Mesoporous Mater.*, 2020, **305**, 110378, DOI: **10.1016/j.micromeso.2020.110378**.

26 F. Xu, Z. F. Bian, T. S. Ge, Y. J. Dai, C. H. Wang and S. Kawi, Analysis on solar energy powered cooling system based on desiccant coated heat exchanger using metal-organic framework, *Energy*, 2019, **177**, 211–221, DOI: **10.1016/j.energy.2019.04.090**.

27 M. M. Mohseni, M. Jouyandeh, S. M. Sajadi, A. Hejna, S. Habibzadeh, A. Mohaddespour, N. Rabiee, H. Daneshgar, O. Akhavan, M. Asadnia, M. Rabiee, S. Ramakrishna, R. Luque and M. R. Saeb, Metal-organic frameworks (MOF) based heat transfer: A comprehensive review, *Chem. Eng. J.*, 2022, **449**, 137700, DOI: **10.1016/j.cej.2022.137700**.

28 G. Férey, C. Mellot-Draznieks, C. Serre, F. Millange, J. Dutour, S. Surblé and I. Margiolaki, A chromium terephthalate-based solid with unusually large pore volumes and surface area, *Science*, 2005, **309**, 2040–2042, DOI: **10.1126/science.1116275**.

29 P. Küsgens, M. Rose, I. Senkovska, H. Fröde, A. Henschel, S. Siegle and S. Kaskel, Characterization of metal-organic frameworks by water adsorption, *Microporous Mesoporous Mater.*, 2009, **120**, 325–330, DOI: **10.1016/j.micromeso.2008.11.020**.

30 J. Ehrenmann, S. K. Henninger and C. Janiak, Water adsorption characteristics of MIL-101 for heat-transformation applications of MOFs, *Eur. J. Inorg. Chem.*, 2011, **4**, 471–474, DOI: **10.1002/ejic.201001156**.

31 P. L. Llewellyn, S. Bourrelly, C. Serre, A. Vimont, M. Daturi, L. Hamon, G. D. Weireld, J. S. Chang, D. Y. Hong, Y. K. Hwang, S. H. Jhung and G. Férey, High uptakes of CO$_2$ and CH$_4$ in mesoporous metal-organic frameworks MIL-100 and MIL-101, *Langmuir*, 2008, **24**, 7245–7250, DOI: **10.1021/la800227x**.

32 S. Xian, J. Peng, Z. Zhang, Q. Xia, H. Wang and Z. Li, Highly enhanced and weakened adsorption properties of two MOFs by water vapor for separation of CO$_2$/CH$_4$ and CO$_2$/N$_2$ binary mixtures, *Chem. Eng. J.*, 2015, **270**, 385–392, DOI: **10.1016/j.cej.2015.02.041**.

33 H. R. Mahdipoor, R. Halladj, E. G. Babakhani, S. Amjad-Iranagh and J. S. Ahari, Adsorption of CO$_2$, N$_2$ and CH$_4$ on a Fe-based metal organic framework, MIL-101(Fe)-NH$_2$, *Colloids Surf., A*, 2021, **619**, 126554, DOI: **10.1016/j.colsurfa.2021.126554**.

34 M. Askarieh, H. Farshidi, A. Rashidi, A. Pourreza and M. S. Alivand, Comparative evaluation of MIL-101(Cr)/calcium alginate composite beads as potential adsorbents for removing water vapor from air, *Sep. Purif. Technol.*, 2022, **291**, 120830, DOI: **10.1016/j.seppur.2022.120830**.

35 L. J. Guo, F. F. Li, J. X. Liu, R. Li, Z. B. Yu, Q. Xi, L. L. Zhang, Y. R. Li and C. M. Fan, Cracked spindle morphology of MIL-101(Fe) for improved photocatalytic nitrogen reduction, *J. Solid State Chem.*, 2022, **316**, 123610, DOI: **10.1016/j.jssc.2022.123610**.

36 P. Horcajada, S. Surble, C. Serre, D. Y. Hong, Y. K. Seo, J. S. Chang, J. M. Greneche, I. Margiolaki and G. Ferey, Synthesis and catalytic properties of MIL-100(Fe), an

iron(III) carboxylate with large pores, *Chem. Commun.*, 2007, 27, 2820–2822, DOI: 10.1039/b704325b.

37 K. Zu, M. Qin and S. Cui, Progress and potential of metal-organic frameworks (MOFs) as novel desiccants for built environment control: A review, *Renewable Sustainable Energy Rev.*, 2020, 133, 110246, DOI: 10.1016/j.rser.2020.110246.

38 K. C. Ng, H. T. Chua, C. Y. Chung, C. H. Loke, T. Kashiwagi, A. Akisawa and B. B. Saha, Experimental investigation of the silica gel–water adsorption isotherm characteristics, *Appl. Therm. Eng.*, 2001, 21, 1631–1642, DOI: 10.1016/s1359-4311(01)00039-4.

39 GB50736-2012, *Design code for heating ventilation and air conditioning of civil buildings*, China construction industry press, Beijing, 2012.

40 GB/T18883-2022, *Standards for indoor air quality*, Standards Press of China, Beijing, 2022.

41 L. Ansone-Bertina, V. Ozols, L. Arbidans, L. Dobkevica, K. Sarsuns, E. Vanags and M. Klavins, Metal–Organic Frameworks (MOFs) containing adsorbents for carbon capture, *Energies*, 2022, 15, 1–33, DOI: 10.3390/en15093473.

42 Y. Liu, J. Zeng, J. Zhang, F. Xu and L. Sun, Improved hydrogen storage in the modified metal-organic frameworks by hydrogen spillover effect, *Int. J. Hydrogen Energy*, 2007, 32, 4005–4010, DOI: 10.1016/j.ijhydene.2007.04.029.

43 Z. Zhang, F. Li, G. Li, R. Li, Y. Wang, Y. Wang, X. Zhang, L. Zhang, F. Li, J. Liu and C. Fan, Cu-doped MIL-101(Fe) with enhanced photocatalytic nitrogen fixation performance, *J. Solid State Chem.*, 2022, 310, 123041, DOI: 10.1016/j.jssc.2022.123041.

44 Q. Xie, Y. Li, Z. Lv, H. Zhou, X. Yang, J. Chen and H. Guo, Effective adsorption and removal of phosphate from aqueous solutions and eutrophic water by Fe-based MOFs of MIL-101, *Sci. Rep.*, 2017, 7, 3316, DOI: 10.1038/s41598-017-03526-x.

45 F. Jeremias, A. Khutia, S. K. Henninger and C. Janiak, MIL-100(Al, Fe) as water adsorbents for heat transformation purposes – a promising application, *J. Mater. Chem.*, 2012, 22, 10148–10151, DOI: 10.1039/c2jm15615f.

46 M. Sohail, Y. N. Yun, E. Lee, S. K. Kim, K. Cho, J. N. Kim, T. W. Kim, J. H. MOON and H. Kim, Synthesis of highly crystalline NH2-MIL-125 (Ti) with S-shaped water isotherms for adsorption heat transformation, *Cryst. Growth Des.*, 2017, 17, 1208–1213, DOI: 10.1021/acs.cgd.6b01597.

47 N. K. Lazaridis, T. D. Karapantsios and D. Georgantas, Kinetic analysis for the removal of a reactive dye from aqueous solution onto hydrotalcite by adsorption, *Water Res.*, 2003, 12, 3023–3033, DOI: 10.1016/S0043-1354(03)00121-0.

48 F. Salman, A. Zengin and H. C. Kazici, Synthesis and characterization of Fe_3O_4-supported metal-organic framework MIL-101(Fe) for a highly selective and sensitive hydrogen peroxide electrochemical sensor, *Ionics*, 2020, 26, 5221–5232, DOI: 10.1007/s11581-020-03601-w.

49 J. B. Huo and G. C. Yu, Mesoporous cerium oxide-anchored magnetic polyhedrons derived from MIL-100(Fe) for enhanced removal of arsenite from aqueous solution, *J. Hazard. Mater.*, 2021, 415, 14, DOI: 10.1016/j.jhazmat.2021.125709.

50 T. K. Trung, N. A. Ramsahye, P. Trens, N. Tanchoux, C. Serre, F. Fajula and G. Férey, Adsorption of C5–C9 hydrocarbons in microporous MOFs MIL-100(Cr) and MIL-101(Cr): A manometric study, *Microporous Mesoporous Mater.*, 2010, 134, 134–140, DOI: 10.1016/j.micromeso.2010.05.018.

51 E. S. Lenoir, C. Vagner, J. W. Yoon, P. Bazin, F. Ragon, Y. K. Hwang, C. Serre, J. S. Chang and P. L. Llewellyn, How water fosters a remarkable 5-fold increase in low-pressure CO_2 uptake within mesoporous MIL-100(Fe), *J. Am. Chem. Soc.*, 2012, 134, 10174–10181, DOI: 10.1021/ja302787x.

52 J. A. Coelho, A. E. O. Lima, A. E. Rodrigues, D. C. Azevedo and S. M. Lucena, Computer simulation of adsorption and sitting of CO_2, N-2, CH_4 and water on a new Al(OH)-fumarate MOF, *Adsorption*, 2017, 23, 423–431, DOI: 10.1007/s10450-017-9872-7.

53 J. Nie, Y. Pang, Y. J. Liu, X. Kong and H. Zhang, Experimental investigation on air dehumidification performance of metal organic frameworks and its application potential for solid desiccant air conditioning systems, *Sci. Technol. Built Environ.*, 2022, 1–11, DOI: 10.1080/23744731.2022.2148822.

54 Z. Rui, Q. Li, Q. Cui, H. Wang, H. Chen and H. Yao, Adsorption refrigeration performance of shaped MIL-101-water working pair, *Chin. J. Chem. Eng.*, 2014, 22, 570–575, DOI: 10.1016/S1004-9541(14)60076-8.

55 Y. K. Seo, J. W. Yoon, J. S. Lee, Y. K. Hwang, C. H. Jun, J. S. Chang, S. Wuttke, P. Bazin, A. Vimont, M. Daturi, S. Bourrelly, P. L. Llewellyn, P. Horcajada, C. Serre and G. Ferey, Energy-efficient dehumidification over hierarchically porous metal-organic frameworks as advanced water adsorbents, *Adv. Mater.*, 2012, 24, 806–810, DOI: 10.1002/adma.201104084.